Hybrid Active PWM Strategy with Dual-Mode Modulation Waves of Three-Level T-type Converter for Aircraft Turboelectric Propulsion Systems

Feng Guo, *Member, IEEE,* Zhuxuan Ma, *Student Member, IEEE,* Fei Diao, *Member, IEEE,* Yue Zhao, *Senior Member, IEEE,* Patrick Wheeler, *Fellow, IEEE*, and Yue Cao, *Senior Member, IEEE*

***Abstract*—Turboelectric propulsion is emerging as an enabling technology for the future aviation industry, aiming to reduce its carbon footprint. To provide electrified thrust for aircraft, the converter-fed motor drive system is a promising solution for the energy conversion between an onboard dc distribution bus and a high-speed electric machine. However, the neutral-point potential fluctuation and even drifting can be an outstanding issue when employing three-level neutral-point-clamped (3L-NPC) topologies, which puts the converter output performance and the lifespan of capacitors at risk. To address these problems, in this paper, a new hybrid active pulse-width-modulation (PWM) strategy is proposed for the studied airborne electric propulsion systems. With the versatile dual-mode modulation signals, not only can the proposed PWM algorithm keep capacitor voltages balanced at the entire range of operating points but also switching losses can be lowered with the help of discontinuous pulse trains during the cruise. Moreover, the computational burden rendered by a short switching cycle is reduced by the sextant coordinate-based analytical derivation. The effectiveness of the presented modulation technique are validated through simulation results from a Simulink/PLECS model and experimental results obtained from a 200 kVA silicon-carbide (SiC) based T-type 3L-NPC prototype with a variable output fundamental frequency.**

***Index Terms*—Coordinate-based, neutral-point voltage, discontinuous pulse trains, turboelectric aircraft propulsion, three-level.**

I. Introduction

THE electric aircraft propulsion technologies result in higher energy conversion efficiency, lower maintenance costs, reduced greenhouse gas emissions, and new methods of aircraft design for the future aviation industry [1]-[3]. To realize these advantages, electric propulsion systems offering electrified thrust attempt to partially or even fully replace their mechanical counterparts. For example, NASA has launched a research project named N3-X with the state-of-the-art superconducting and turboelectric technologies, where the 14 propulsive fans can provide up to 25 MW thrust power during takeoff [4]. Though the all-electric-aircraft (AEA) concept leads to zero carbon footprint, the turboelectric distributed propulsion (TeDP) based aircraft is more viable in the near term because of fewer technical and economic barriers. One of the convincing cases is the STARC-ABL by NASA [5], where an aft motor-driven fan fed by 2 to 3 MW generators provides electrified thrust for the aircraft.

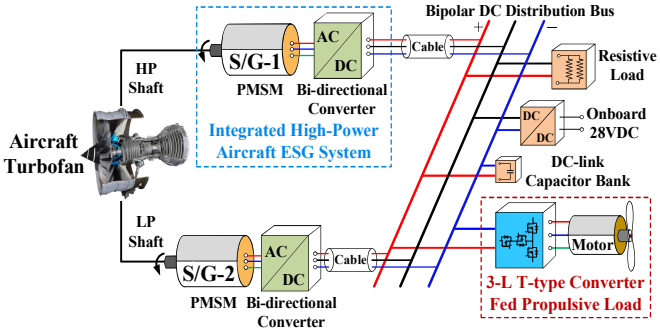

Fig. 1. Configuration of the advanced aircraft TeDP system.

To increase the penetration of electrical systems on the aircraft, an advanced TeDP system fed by integrated electric starter/generator (ESG) systems is proposed, as shown in Fig.1. In comparison with the original turboelectric powertrain, the functionality of aircraft engine startup is added without the use of the auxiliary power unit (APU). Two sets of high-power permanent magnet synchronous machines (PMSMs) and bi-directional active front ends (AFEs) take power from the main engine via high pressure (HP) and low pressure (LP) shafts. To raise the output power of electrified thrust, this dual-channel power generation center transfers power to the electric power system (EPS) altogether. While the $\pm$ 270 V is still the highest standard voltage for the existing aircraft systems, the medium-voltage dc distribution (MVDC), such as $\pm$ 2 kV for N3-X, is preferable as the weight of the power cable can be reduced significantly. Considering other onboard avionic loads, here, a bipolar dc-bus architecture of $\pm$ 540 V is chosen as a candidate so that the requirements for propulsive and non-propulsive loads can be satisfied all at once. Furthermore, it is noteworthy that not only can the dc distribution with an elevated voltage standard improve the efficiency of electrical machines but also enables an operating point of a higher power factor (PF) during the cruise. These becomes a paradigm for the latest electrified aircraft propulsion applications [6]-[8]. Owing to low electromagnetic interference (EMI) emission and enhanced power quality, the three-level (3-L) converter, instead of its two-level counterpart, could be utilized to drive an MW-class motor for the thrust generation. With the maturity of the high-performance wide bandgap (WBG) semiconductor, the silicon-carbide (SiC) based 3-L T-type converter (T^2C) illustrated in Fig.2 is prototyped to investigate the aircraft TeDP system. This circuit deploys the minimum count of

This work was supported in part by the U.S. National Science Foundation (NSF) under CAREER Award ECCS-1751506.

Feng Guo, Zhuxuan Ma, Fei Diao and Yue Zhao are with the Power Electronic System Laboratory at Arkansas (PESLA), Department of Electrical Engineering, University of Arkansas, Fayetteville, AR 72701, USA (email: fengg@uark.edu; zm009@uark.edu; feidiao@uark.edu; yuezhao@uark.edu)

Patrick Wheeler is with the Power Electronics, Machines, and Control Research Group, University of Nottingham, NG7 2RD Nottingham, U.K. (email: pat.wheeler@nottingham.ac.uk)

Yue Cao is with the School of Electrical Engineering and Computer Science, Oregon State University, Corvallis, OR 97331, USA. (email: yue.cao@oregonstate.edu)

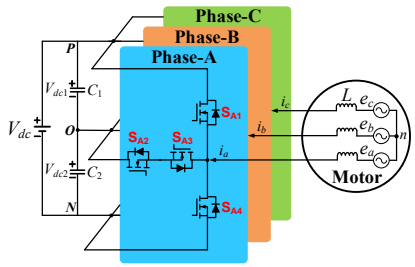

Fig. 2. Schematic of 3-L T^{2}C-fed electric propulsion motor.

switches compared with other 3-L topologies, such as the active-neutral-point-clamped (ANPC) converter [9].

Since the 3-L T^{2}C plays a significant role in the energy flow of the TeDP system, its performance affects the efficiency and reliability of entire airborne facilities. Nevertheless, one of the prominent drawbacks of the NPC topology is the neutral-point (NP) potential deviation caused by the split dc-link capacitors, which jeopardizes capacitor bank lifetime, increases ac output harmonics and over-stresses SiC devices. Though the imbalance can be rectified to some extent in particular situations by the self-equilibrium phenomenon [10], stringent requirements of system parameters might be hardly fulfilled, and its recovery process is not prompt. Another solution to this problem is to use auxiliary circuits across the capacitors, such as two extra isolated dc sources [11], while the added weight and volume might be prohibitive to be adopted for aerospace applications. By contrast, without any hardware-level efforts, the pulse-wide-modulation (PWM) technique with active NP voltage balancing emerges as a simple but powerful alternative.

In the existing literature, there are two major categories of PWM strategies, i.e., the space-vector modulation (SVM) and the carried-based (CB) modulation, for the 3L-NPC converter. In the SVM category, the nearest-three virtual-space-vector (NTV^2) in [12] is much more suitable for perfect NP potential balance in those applications of high modulation index (MI) and low PF. The reason for that is an average zero NP current can be obtained in every switching period. This concept is followed by the continuous research in [13], [14] to maintain NP voltage balanced after perturbation, even under overmodulation conditions [15]. Moreover, the common-mode voltage (CMV) can be alleviated by deploying the optimal switching states [16]-[18]. Along with the increased equivalent switching frequency, additional switching losses undermine its benefit. Hence, quite a few SVM solutions with nearest-three-vector (NTV) outputs have been reported, as referred to [19]-[21], which are helpful for the NP potential fluctuation elimination, CMV attenuation and less thermal stress. Apart from these methods, with the help of the non-linear control, such as the sliding-mode control (SMC) [22] and the model predictive control (MPC) [23], system dynamic performance is improved as a premise of NP voltage balance. Due to high computation burden, however, the implementation of SVM could be less competitive for multilevel topologies, particularly for those using WBG technologies with a high switching frequency.

In contrast, the simplicity of the CBPWM scheme is realized by a comparison between the modulation signal and the carrier waveform. Novelties come from the re-arrangement of modulation signals [24]-[26] or carriers [27] for balancing capacitor voltages or suppressing CMV magnitude. On other hand, creativity comes with the injected zero-sequence voltage (ZSV) that generates dedicated pulse trains. In [28], the authors introduce a CBPWM with flexible ZSV injection to correct NP potential error and lower the switching loss, followed by presenting zero-sequence components to extend the output capability of the traction inverter in the overmodulation region [29]. Adopting two types of ZSVs alternatively [30], two discontinuous PWM (DPWM) solutions that are beneficial for reducing switching loss toggle back and forth if capacitor voltages deviate. Nevertheless, an appropriate ZSV is not always easy to determine. One possible path is to derive modulation waves from the known switching patterns, which evolves a type of hybrid PWM technique incorporating SVM and CBPWM features. In the works of [31], aiming for electric vehicle (EV) applications, duty cycles of redundant switching states by the NTV are calculated from a single carrier wave to balance NP voltage and reduce switching actions. In [32], with a single virtual carrier, modulation waves of the NTV scheme are derived. In [33], with the vector-shifted method, NTVs are equivalently generated by modulated signals. To settle the low carrier ratio issue, using the inverse operation of NTV scheme, a synchronized CBPWM is proposed by authors of [34]. In [35], by the PWM model of the 3L-NPC, a NTV^2-based CBPWM is introduced. Nonetheless, these attempts are all established from the a-b-c reference frame perspective and rely on the resultant three variables, thus lacking intuitive correspondence in the vector space named as space-domain. Though the works of [36] explore a hybrid PWM on a basis of the sextant plane, setting out a simple implementation of the NTV^2 for the ESG system with lower PFs, all merits are at the expense of extra switching losses. Therefore, its core modulation concept may not be optimal for the target systems with a profile of a higher load angle anymore.

In this paper, a hybrid active PWM strategy with dual-mode modulation waves is proposed for the 3-L T^{2}C in the studied aircraft TeDP systems. Compared with the basic theoretical analysis and preliminary results of this work initially presented in [37], the major contributions of the introduced modulation technique are given as follows: 1) The equivalence between the NTV scheme and CBPWM scheme is revealed under the sextant-coordinate system, thereby leading to a new hybrid modulation algorithm. 2) The space-vector coordinate-based ZSVs that bridge the space-domain and time-domain are strictly derived to streamline the proposed PWM method, which offers CBPWM an extra degree of freedom. 3) With flexible modulation signals, the versatile pulse patterns enabling DPWM can be generated during the long-range cruise flight, which aims to realize capacitor voltage balancing, switching loss reduction and NP potential ripple suppression at the same time.

The rest of this paper is organized as follows. The principles of the aircraft TeDP system are briefly introduced in Section II. The proposed hybrid PWM algorithm, along with the capacitor voltage balancing control, dual-mode pulse train generation, and dedicated coordinate-based ZSV derivation, is presented in Section III. The effectiveness and feasibility of this modulation strategy are verified by the simulation and

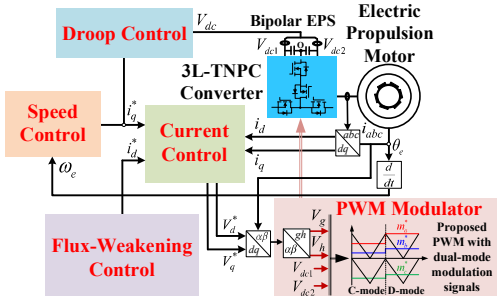

Fig. 3. Control blocks of the developed TeDP system.

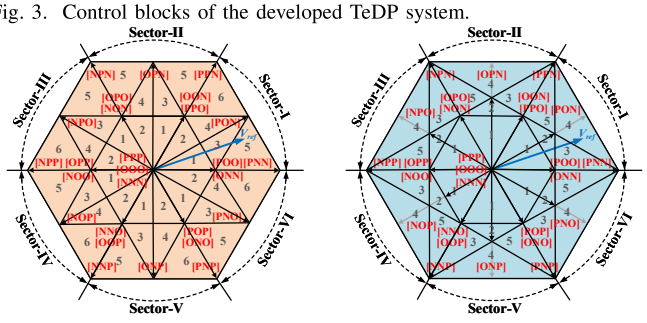

(a) (b)

Fig. 4. The space-vector diagram of: (a) NTV scheme. (b) NTV^2 scheme.

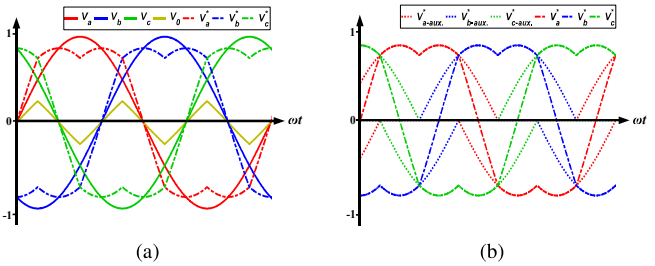

(a) (b)

Fig. 5. The modulation signals of: (a) the conventional CBPWM scheme. (b) the NTV^2-based CBPWM scheme.

experimental results in Sections IV and V, respectively. Finally, The main conclusions of this work are drawn in Section VI.

II. Principles of Aircraft TeDP System

A. Control Design of TeDP System

Fig.3 presents the control block diagram of the developed TeDP system that involves machine speed control, flux-weakening control, dc-link current control and PWM modulator. The speed control is enabled throughout the flight. The vector control technique is used for machine decoupling purposes, which allows controlling flux and torque independently. As a result, machine torque represented as active power is controlled by q-axis current. To regulate the current of bipolar dc distribution bus, droop characteristics are required to consider in the control design. A negative d-axis current may be injected if an immense amount of propulsive power is needed when the aircraft executes a go-around accidentally. It is worth noting that the q-axis current is constantly required during the cruise, which generates active power for electric thrust. The PWM scheme is responsible for producing advanced pulse trains in order to deliver electricity to drive propellers.

B. Three-Level T-type NPC Topology, SVM and CBPWM Strategies, and Associated Modulation Issues

The main circuit of the 3-L T^{2}C is shown in Fig.2. As shown, each phase consists of two switches (S_{x1} and S_{x4}) in the normal half-bridge (HB) configuration and two switches

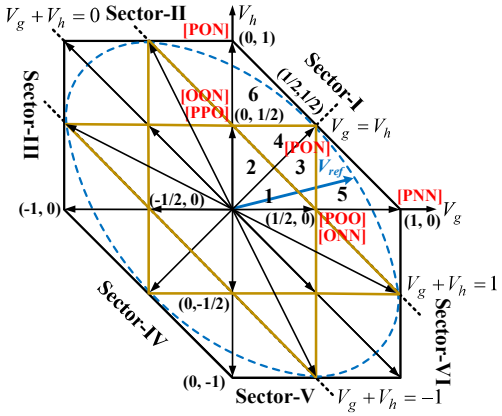

Fig. 6. SVD of the NTV scheme with the g-h coordinate system.

TABLE I
Switching Principle of The 3-L T^{2}C

Switching States	Gating Signals (S_{x1},S_{x2})	Output Voltages
[P]	(1, 1)	$V_{dc}/2$
[O]	(0, 1)	0
[N]	(0, 0)	$-V_{dc}/2$

(S_{x2} and S_{x3}) in the common-source (CS) configuration, where x={A, B, C}. The gating signal of S_{x1} is complementary to that of S_{x3}. Also, S_{x2} and S_{x4} follow the same manner. Two identical capacitors (C_1 and C_2) are series-connected to form the dc-link. For this topology, there are 27 switching states generated in total. When S_{x1} and S_{x2} are turned on, the switching state is represented as [P], with output voltage $V_{dc}/2$. The switching state [O] indicates that both switches in the CS configuration are turned on, corresponding to the null output voltage. The switching state [N] means that S_{x3} and S_{x4} are turned on and produces $-V_{dc}/2$ of the output voltage. The switching principle can be found in Table I. The combination of these states formulates zero, small, medium and large vectors approximating reference voltage command.

The division of the symmetric NTV strategy results in 6 subsectors in each sector. If the reference voltage vector falls into the subsector-5 in Sector-I, the NTV with four switching states, i.e., [POO], [ONN], [PON] and [PNN], are deployed to synthesize V_{ref}, as shown in Fig.4(a). However, due to the predominant participation of medium vectors, the NP potential imbalance occurs. By contrast, the repartition of the original NTV^2 strategy results in 5 subsectors in each sector. Assuming that the reference voltage vector is located in the subsector-4 of Sector-I. To compose V_{ref}, a virtual space-vector, as a specific proportion of [ONN], [PON] and [PPO], is used together with [PPN] and [PNN], as given in Fig.4(b). Due to average-zero NP current over a switching cycle, this scheme achieves perfect NP voltage balance, particularly fitting for low PF scenarios. Given that the TeDP systems seldom induce a lower load angle, and the advantage of balanced NP voltage is taken at the expense of an increased switching loss of 33% [34], the NTV^2 might not be the suitable PWM candidate.

The CBPWM generates pulse trains with a comparison between sinusoidal modulation signals, denoted as $V_{a\sim c}$, and level-shifted carriers. To boost dc-bus voltage utilization ratio, by (1), a ZSV in the time-domain component, denoted as V_0, is

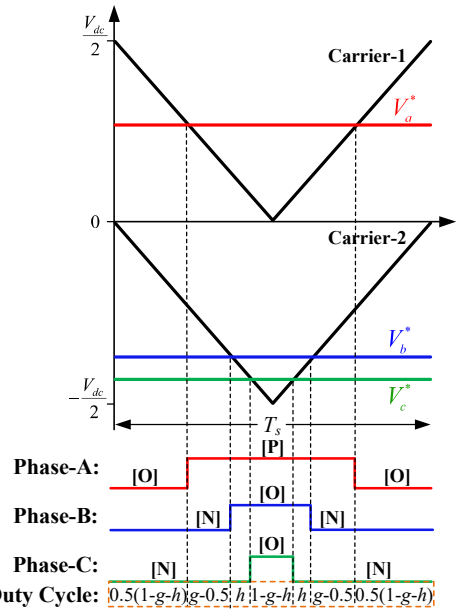

Fig. 7. The relationship between modulation waves and switching patterns under the g-h reference frame for subsector-5 of Sector-I.

injected, as presented in Fig.5(a). To attain the 3-L switching intervals as same as the NTV^2, two auxiliary signals are required in specific instants, as shown in Fig.5(b). Likewise, these extra switching actions are unfavorable for the efficiency of the high-power converter in the target propulsion drives.

$$V_0 = -\frac{\max(V_a, V_b, V_c) + \min(V_a, V_b, V_c)}{2} \tag{1}$$

C. Simplified SVM with Sextant Coordinate System

To simplify the SVM process, by (2), algebraic operations of dwell time are adopted to reduce computational costs of the NTV^2 strategy for the 3L-NPC topology [18]. As for the NTV counterpart, its modified hexagonal space-vector diagram (SVD) under the g-h reference frame is illustrated in Fig.6.

$$\begin{bmatrix} V_g \\ V_h \end{bmatrix} = \begin{bmatrix} 1 & -1/\sqrt{3} \\ 0 & 2/\sqrt{3} \end{bmatrix} \begin{bmatrix} V_\alpha \\ V_\beta \end{bmatrix} \tag{2}$$

It is worth noting that the linear programming of associated coordinate sets can easily identify sector and subsector. Also, dwell times of switching states are expressed as functions of coordinates. These features inspires us to migrate the space-vector coordinate to the modulation waves, which paves the way for presenting the proposed hybrid PWM afterward.

III. Proposed Hybrid Active PWM Strategy with Dual-Mode Modulation Waves

In the following text, the presented hybrid active PWM technique with dual-mode modulation waves is elaborated in each subsection. Without loss of generality, the first sector is chosen as a representative example to explain.

A. Analytical Analysis of Space-Vector Coordinate and Associated Modulation Waves

Assuming that the reference voltage vector is located in subsector-5 of Sector-I, as given in Fig.4(a), the modulation waves and associated switching patterns equivalently generated by the SVM scheme are shown in Fig.7. With the help of similar triangles, the following equations can be attained:

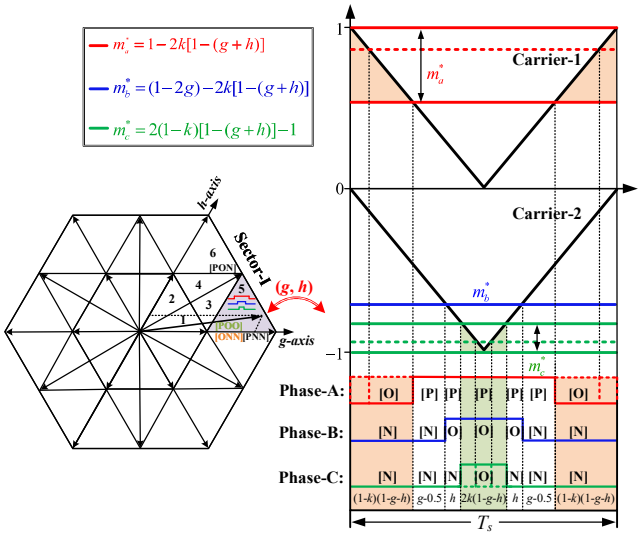

Fig. 8. The dual-mode modulation waves generation of the proposed hybrid active PWM strategy in the subsector-5 of Sector-I.

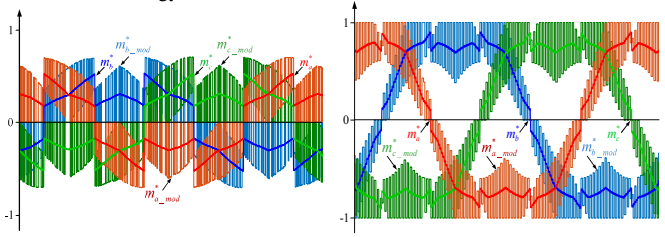

(a) (b)

Fig. 9. Three-phase modulation waveforms by the proposed hybrid active PWM strategy with continuous and discontinuous switching pattern under: (a) MI=0.4 and (b) MI=0.9.

$$\begin{cases} \dfrac{2V_a^*}{V_{dc}} = \dfrac{T_s/2 - (1-g-h)\cdot T_s/2}{T_s/2} \\ \dfrac{2V_b^*}{-V_{dc}} = \dfrac{[(1-g-h)/2 + (g-1/2)]\cdot T_s}{T_s/2} \\ \dfrac{2V_c^*}{-V_{dc}} = \dfrac{[(1-g-h)/2 + (g-1/2) + h]\cdot T_s}{T_s} \end{cases} \tag{3}$$

where V_a^*, V_b^* and V_c^* indicate three-phase modulation waves, T_s refers to a switching period, and V_{dc} is the dc-bus voltage.

If the modulation waves are normalized with half of the dc-bus voltage, then g-h coordinate-based modulation signals, denoted by m_a^*, m_b^* and m_c^*, can be simply yielded as:

$$\begin{cases} m_a^* = g + h \\ m_b^* = h - g \\ m_c^* = -(g+h) \end{cases} \tag{4}$$

With a similar derivation for the functions of coordinate-based dwell time, the resultant modulation signals establish the basis of the proposed hybrid PWM algorithm in this paper.

B. NP Potential Balancing Control

As a pair of the small vector is projected into modulation waves, a straightforward solution from the perspective of SVM to maintain NP potential at a balanced condition is to dynamically manipulate the dwell time of P- and N-type small vectors. In other words, to realize an equivalent adjustable switching pattern in the time-domain, the coordinate-based modulation waves offset dc-bias in the NP with a voltage-domain regulation, thus producing scalable coordinates for the

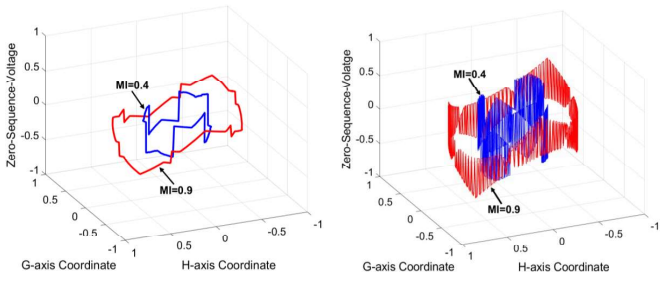

Fig. 10. The 3D-trajectory plots of injected ZSVs as a function of g- and h-axis coordinate over a fundamental cycle in the case of: (a) Balanced NP potential state and (b) Unbalanced NP potential state.

hybrid active modulation strategy. The coefficient k representing capacitor voltage divergence is defined in (5). If k equals 0.5, it means that two capacitor voltages are well balanced.

$$k = \frac{V_{dc1}}{V_{dc1} + V_{dc2}} \in [0, 1] \tag{5}$$

Here, subsector-5 of the first sextant is still taken as an example to explain the introduced NP potential balancing control method. In order to recover the imbalance, the duty cycle of [ONN] and [POO] are compensated as $2(1-k)(1-g-h)$ and $2k(1-g-h)$, respectively, as illustrated in Fig.8. Accordingly, three-phase modified modulation signals, represented as $m^*_{a\_mod}$, $m^*_{b\_mod}$ and $m^*_{c\_mod}$, are expressed as follows:

$$\begin{cases} m^*_{a\_mod} = 1 - 2k \cdot [1 - (g + h)] \\ m^*_{b\_mod} = (1 - 2g) - 2k \cdot [1 - (g + h)] \\ m^*_{c\_mod} = 2(1 - k) \cdot [1 - (g + h)] - 1 \end{cases} \tag{6}$$

C. Discontinuous Pulse Trains Generation

It can be seen from Fig.8 that the modulation waves of phase-A and C take initiative to dynamically regulate if the NP potential drifts away from zero. Consequently, there is a scenario where a P- or N-type small vector is removed in every switching period. This indicates that the center-aligned seven-segment PWM omits two switching actions, resulting in five-segment pulse trains. In order to realize such discontinuous switching patterns for the proposed hybrid active PWM, the coefficient k is required to be bounced back between 0 and 1. One of the simple implementations is to employ a feedback hysteresis loop of NP potential bias so that only one type of small vector takes effect in every PWM interrupt service routine. Accordingly, in terms of the presented modulation technique of the studied TeDP systems, its continuous pulse train (C-mode) shifts to a discontinuous counterpart (D-mode).

Fig.9 shows generated three-phase modulation signals with the C and D-mode pulse trains under unity PF and two different MI. As can be observed from Fig.9(a), at a MI of 0.4, more PWM intervals periodically stay at zero-state to avoid unnecessary switching actions. Hence, the output voltages of corresponding phase leg clamp to the NP, indicating a lower dc-bus voltage utilization, which refers to the rotation speed ramping-up stage of the electric motor. When the studied propulsion drives operate at the steady-state with a high speed at the cruising stage, the operating condition of a higher dc-bus voltage utilization is required. This means that the output

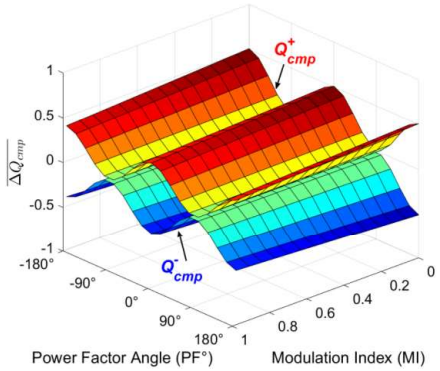

Fig. 11. Normalized NP charge compensation at different MI and PF.

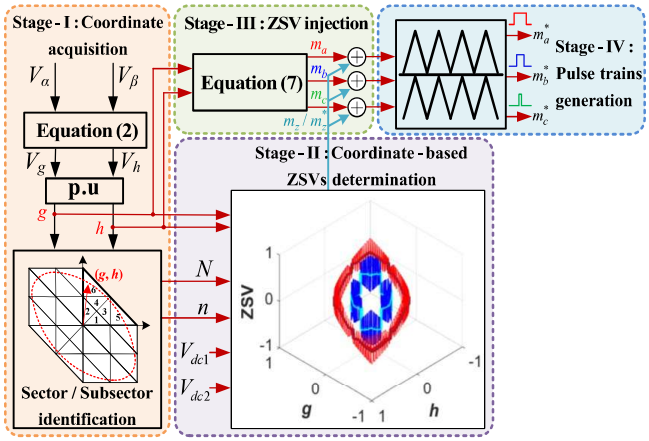

Fig. 12. Flowchart of the proposed hybrid active PWM technique with dual-mode modulation waves.

voltage of the 3-L T^{2}C will primarily clamp to the positive and negative dc-rail, which corresponds to the case of Fig.9(b).

D. Coordinated-Based Zero-Sequence Voltage Analysis

To reveal the mechanism of ZSV injection for the presented hybrid active PWM, three-phase sinusoidal reference voltages as the output of current control loop would be projected into the sextant plane. The transformation matrix is given by:

$$\begin{bmatrix} m_a \\ m_b \\ m_c \end{bmatrix} = \begin{bmatrix} 1 & 1/2 \\ -1/2 & 1/2 \\ -1/2 & -1 \end{bmatrix} \begin{bmatrix} g \\ h \end{bmatrix} \tag{7}$$

where m_a, m_b and m_c refer to the components of the reference voltage vector in the a-b-c coordinate system.

In accordance with (4) and (7), the dedicated ZSV demand, denoted as m_z, for subsector-5 of Sector-I under balanced NP voltage can be thus calculated by (8). Once NP potential drifts away from zero, active ZSVs, represented as m^*_z, participate in correcting imbalance, which can be derived in (9). It is apparent that (8) is satisfied if k equals 0.5.

$$m_z = h/3 - g/3 \tag{8}$$

$$m^*_z = (1 - 2k) + (2k - 4/3) \cdot g + (2k - 2/3) \cdot h \tag{9}$$

Together with similar algebraic relationships fitting for all sectors, the 3D-trajectory plots of ZSVs under different NP potential states is illustrated in Fig.10. As shown in Fig.10(a), which differs from the time-domain ZSV displayed in Fig.5(a) for the conventional CBPWM, two decoupled variables inherited from the SVM concept that signifies the vertex of reference voltage vector can precisely determine the amount

of zero-sequence component. As for a MI of 0.4 and 0.9, Fig.10(b) shows the injected ZSVs with designated polarities in the case of deviated capacitor voltage convergence process.

E. Capacitor Voltage Balancing Performance Analysis

To evaluate the NP voltage balance control performance, the compensated electric charge to correct the imbalance in subsector-5 of Sector-I, denoted as ΔQ_{cmp}, can be calculated:

$$\begin{aligned}\Delta Q_{cmp} = 2(1-2k)\cdot[1 - m\sin(\frac{\pi}{3}-\theta) \\ -m\sin(\theta)]\cdot I_{rms}\cdot T_s\cdot\cos(\theta-\varphi)\end{aligned} \tag{10}$$

where m refers to the MI, θ indicates a reference voltage vector rotating angle, I_{rms} manifests the phase current root-mean-square (RMS) value, and φ denotes the load angle.

Through a similar derivation among other subsectors over a fundamental period, the average active NP voltage balancing control capability can be yielded as:

$$\overline{\frac{\Delta Q_{cmp}}{I_{rms}T_s}} = \frac{1}{2\pi}\int_0^{2\pi}\frac{\Delta Q_{cmp}(\theta)}{I_{rms}T_s}\cdot d\theta \tag{11}$$

From the above analysis, it is known that, when the P or N-type small vector is solely employed, the maximum NP voltage balance capability can be gained, which corresponds to the D-mode. Fig.11 plots the generated electric charges that are normalized with the maximum amount expressed as a function of MI and PF. As shown, the positive and negative electric charges, denoted as Q^+_{cmp} and Q^-_{cmp}, are holistically provided by the proposed method. Also, it is evident that the ability to merge the capacitor voltage difference is decreased gradually when the PF towards $\pm$ 90°. In view of operating conditions of adjacent unity MI and high PF for the studied propulsion drives, particularly at the cruise, the proposed modulation technique is able to restore NP voltage at a balanced state.

Fig.12 presents the flowchart of the proposed hybrid active PWM supplemented by dual-mode modulation waves.

IV. Simulation Results

A simulation model for a 3-L T^{2}C in the developed MW-scale advanced aircraft TeDP architecture is built in the PLECS blockset embedded within the Simulink environment under RL load conditions, and the parameters are detailed in Table II. To verify the performance of correcting NP potential drift, output distortion and power losses of the proposed PWM, the conventional CBPWM and NTV^2-based CBPWM are chosen as the benchmark in the following. The operating conditions with two sets of fundamental frequencies, modulation indices and power factors, referring to the startup and steady propulsion stage of the target systems, are carried out in the simulations.

A. Capacitor Voltage Balancing Capability

At a fundamental frequency (f_0) of 400 Hz within the system startup process, two capacitor voltages are initially set at 535 V and 545 V under the benchmark method. Though a 10 V bias in the NP is not too large, a proof of concept can be fulfilled, even for the following D-mode activities under an imbalance state. The corresponding MI and PF of the TeDP system are 0.4 and 0.9, respectively. As shown in Fig.13, with the NTV scheme, NP voltage is in a drifted condition and low-frequency NP potential ripple is large. While the NTV^2-based CBPWM eliminates this undesirable ripple, the NP voltage error is still existed. When switching to the proposed PWM algorithm, dual-mode operations are shown to verify the ability of NP potential convergence. For the C-mode, an error of 10 V in the NP is effectively corrected, and so is the subsequent D-mode. Fig.14 presents the steady-state with a MI of 0.95, PF of 0.75 and f_0 of 1 kHz. A low load angle is adopted here as this operating point indicates a case under a large flex-weakening current injection. As shown, the existed NP voltage deviation is removed. Furthermore, for the above operating points, not only do two capacitor voltages remain balanced by the proposed hybrid active PWM with D-mode but also the magnitude of NP potential ripple is notably suppressed.

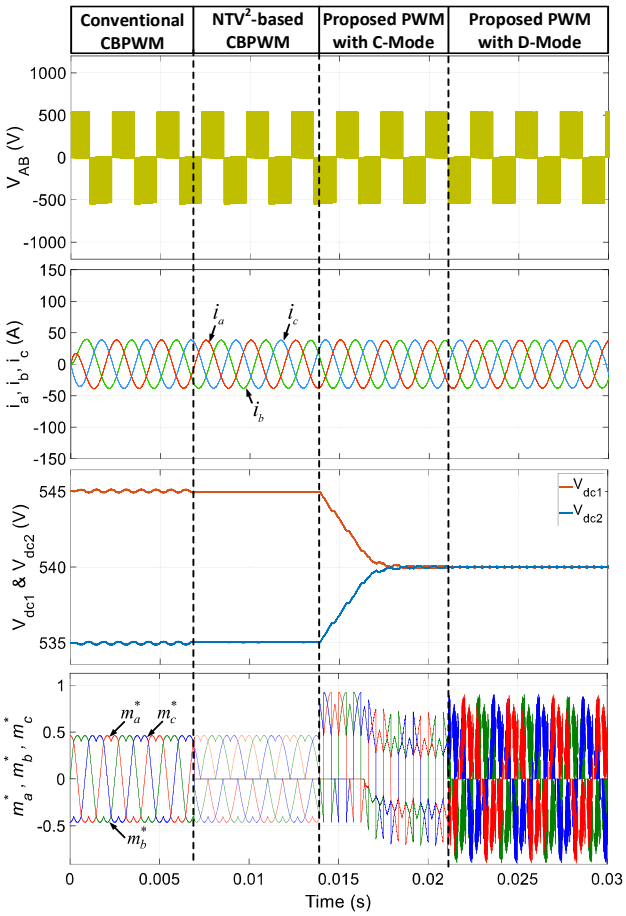

Fig. 13. Simulation results for the studied TeDP system executing the startup process (MI=0.4, PF=0.9 and f_0=400 Hz).

B. Output Variables Performance

With respect to the current in Phase-A, the THD of the above two operating points is 2.13% and 2.55% by the conventional CBPWM scheme, and is 2.12% and 2.53% by the proposed hybrid PWM sending active continuous pulse trains. When the the NTV^2-based CBPWM is employed, that value increases to 2.71% and 2.94%, respectively. By contrast, when the proposed hybrid PWM sending active discontinuous pulse trains trigger, it results in a further rise with 2.98% and 3.15%. As for the modulated signals of the presented hybrid PWM, it is evident from Fig.13 and Fig.14 that, regardless of the operating status of the TeDP system, dual-mode modulation waves work well for the applied 3-L T^{2}C, which clamps ac output voltage to the NP, positive/negative dc-rail effectively.

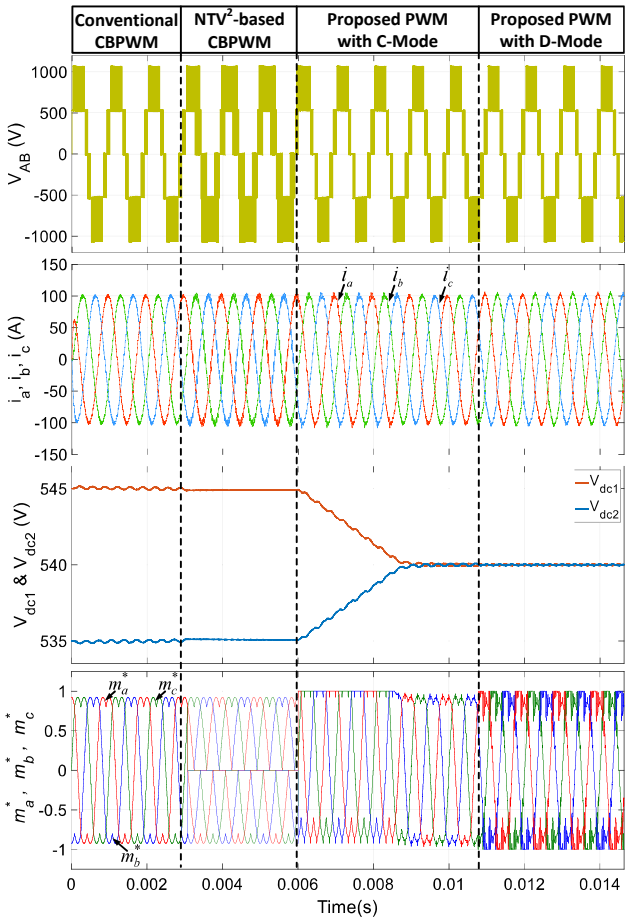

Fig. 14. Simulation results for the studied TeDP system generating the steady thrust process (MI=0.95, PF=0.75 and f_0=1 kHz).

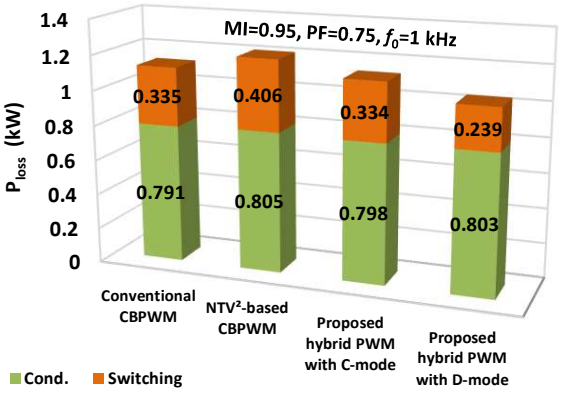

Fig. 15. Comparison of power loss breakdown under the benchmark method and the proposed hybrid active PWM algorithm.

C. Power Loss Analysis

To consist with the hereafter experiments, Cree/Wolfspeed HT-3000 series 900 V silicon-carbide (SiC) module that builds for the 3-L T^{2}C prototype is chosen to analyze semiconductor losses produced by the proposed modulation strategy in the steady-state of the TeDP system. The selected power module features the following parameters: drain-source resistance ($R_{DS(on)}$) is 1.25 mΩ at a gate-source voltage (V_{GS}) of 15 V and a continuous drain current (I_D) of 600 A, turn-on/off switching energy (E_{on}/E_{off}) are 18.5 mJ and 12.5 mJ at 25°C, a drain-source voltage (VDS) of 900 V, and a gate resistance (R_G) of 2 Ω, respectively, the gate to source charge (Q_{gs}) and gate to drain charge (Q_{gd}) are 544 nC and 640 nC, respectively. The switching frequency is set at 30 kHz, the dc-bus voltage is ± 250 V and the power rating is 200 kVA. By using characteristic curves from the manufacturer's datasheet which contains energy dissipation in every turn-on (E_{on}) and turn-off (E_{off}) of the semiconductor as a function of the current and under a given V_{GS}, the power losses are calculated by the PLECS simulation tools.

In Fig.15, the comparison of conduction and switching losses breakdown is given by the benchmark method and the proposed solutions at the steady-state of the TeDP system. It can be found that, as a result of fewer switching actions, the total amount of loss by the proposed hybrid PWM approach with D-mode is the lowest among the others, whereas the C-mode lead to a similar amount of loss compared with the conventional CBPWM scheme. Because of 3-L output phase voltages over a switching period, the NTV^2-based CBPWM scheme faces up to more severe thermal stress issues.

D. Comparison With Other Three-Level Hybrid PWM

Compared with the existing hybrid modulation strategies for the 3L-NPC topology in the literature, the proposed PWM algorithm attributes the following attractive features:

1) To realize the hybrid pulse trains, five logical control blocks assist to generate gating signals for switching loss reduction [31]. In this regard, dual-mode PWM in this study is easier to implement with streamlined modulation processes.

2) The presented modulation technique tightly bonds the concept of space vector and ZSV by means of the g-h coordinate. However, in the works of [32], three control objectives derived from the a-b-c coordinate system are required to generate equivalent switching patterns of the SVM.

3) By leveraging small vector pairs and regulating their coordinate-based modulation signals, the capacitor voltage deviation, even NP potential ripple, can be addressed significantly. In this key aspect, the works of [33] fail to settle properly.

4) Since trigonometric operations are utilized in [34], the massive computational effort to generate hybrid PWM is inevitable, particularly for a dedicated SVM with multi-segment switching patterns, while algebraic operations adopted in this research overcome this issue effectively.

5) The presented DPWM-enabling modulation waves are beneficial for switching loss reduction. Therefore, the improved overall efficiency of the 3-L T^{2}C would be expected when thrusting the aircraft electrically. By contrast, the solution in [35] suffers from thermal issues.

6) Unlike only using coordinate-based modulation signals, yielded as a form of ZSV superposition, which implements the modified NTV^2 [36], the proposed ZSV injection method in the space domain refines the modulation process further.

Meanwhile, it is worth noting that the D-mode of the proposed hybrid PWM strategy leverages the dc-rail clamping pulse pattern to lower switching action. In comparison with the continuous PWM, however, distortion on output variables is inevitably increased as a result of exploit of the non-NTV.

V. Experimental Results

Before an MW-scale high-speed electric propulsion motor is available to serve as the load to investigate the modulation

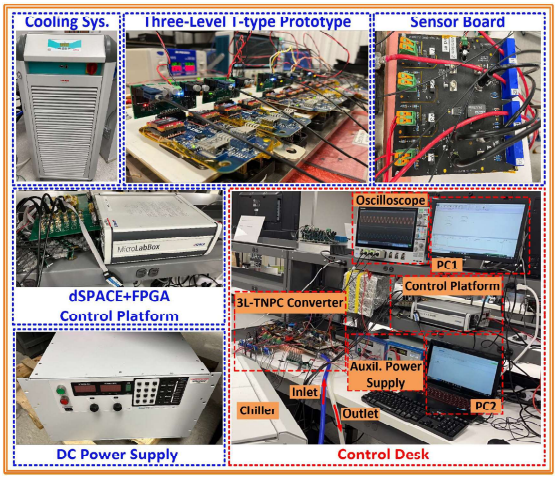

Fig. 16. Experimental test rigs.

TABLE II
AIRCRAFT TEDP SYSTEM PARAMETERS

Parameters	Simulation	Experimentation
Rated power	1000 kVA	200 kVA
DC-bus voltage	± 540 V	± 250 V
Switching frequency	30 kHz	30 kHz
Fundamental frequency (f_0)	≤ 1 kHz	≤ 1 kHz
Capacitance (C_1=C_2)	900 μF	300 μF
Modulation index (MI)	≤ 0.95	≤ 0.95
Power factor (PF)	0.7∼1.0	0.7∼1.0

performance of the proposed hybrid PWM technique with dual-mode modulation waves, the presented algorithm is experimentally validated on a scaled-down 200 kVA SiC-based T-type 3L-NPC prototype for aircraft turboelectric propulsion applications, as shown in Fig.16. Table II details the specifications. A Magna-Power TSD4000-5/208+LXI programmable dc power supply is connected to the positive and negative dc-rail of the converter and an RL load bank is connected to its ac side, which imitates the aircraft onboard EPS and load angles of assumed high-power density electric propulsion motor, respectively. A cold plate installed underneath the converter along with a Julabo FL2503 supplying recirculating chilled water consists of the cooling system of the prototype. The control platform includes a dSPACE MicroLabBox and an Intel Max-10 FPGA. The parameters of ac side are monitored by a Yokogawa WT5000 precision power analyzer. As the direction of phase current changes rapidly in light-load conditions, it impairs the NP potential drift correction capability. Thus, the experimental tests mainly focus on the TeDP system operating in a light-load condition with a variable f_0. All the variables are measured by high voltage differential probes and A622 current probes connected on a Tektronix oscilloscope.

A. Initial Capacitor Voltage Imbalance

Fig.17 shows the two capacitor voltages (V_{dc1}/V_{dc2}), line current and phase voltage when the proposed PWM is instantly enabled at the operating point of the aircraft cruising stage, i.e., a MI of 0.95 and PF of 0.75 for the TeDP systems. As seen from Fig.17(a), a NP potential bias of 45 V exists under the conventional CBPWM scheme, which leads to a distorted line-to-line voltage. However, the imbalance can be recovered within 8.78ms when the proposed hybrid PWM with

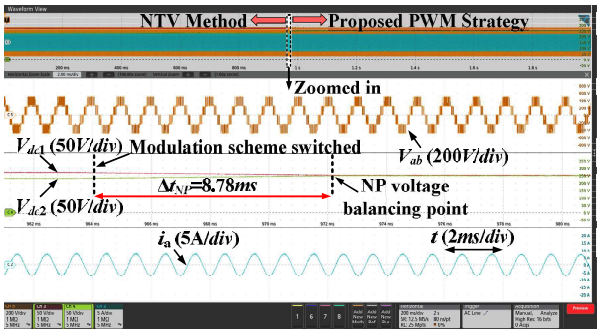

(a)

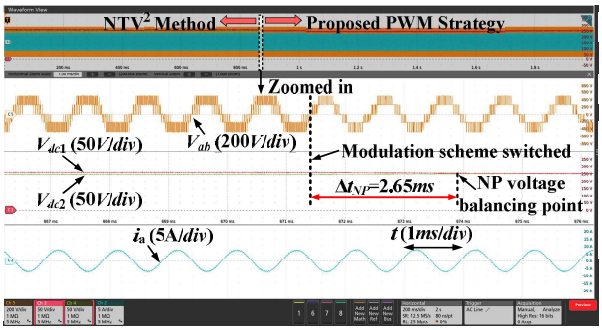

(b)

Fig. 17. NP voltage balance performance of the proposed hybrid active PWM compared with: (a) The conventional CBPWM (b) The NTV^2-based CBPWM.

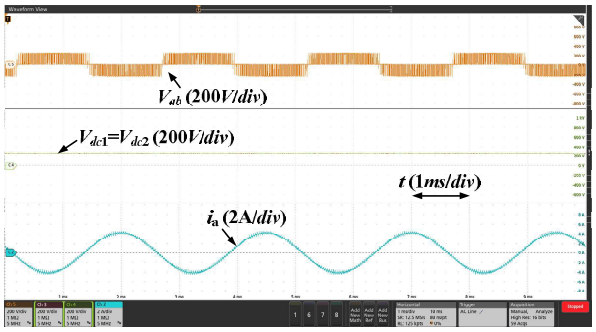

(a)

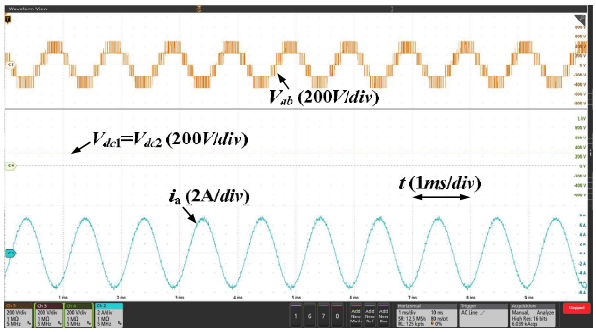

(b)

Fig. 18. The steady-state modulation performance of the proposed hybrid active PWM under: (a) f_0=400 Hz and (b) f_0=1 kHz.

discontinuous pulse train is employed. Furthermore, as a result of the non-ideal switching characteristics, the NP potential drifts under the NTV^2 scheme, but the shifted NP voltage are shortly kept in a balanced state again under the hybrid PWM with continuous pulse train, as shown in Fig.17(b). The above results validate the well-performed NP voltage balance ability of the introduced modulation algorithm.

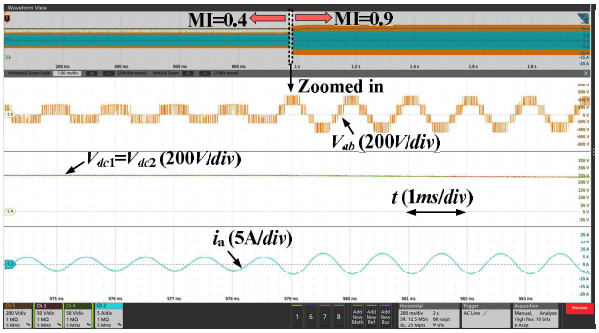

(a)

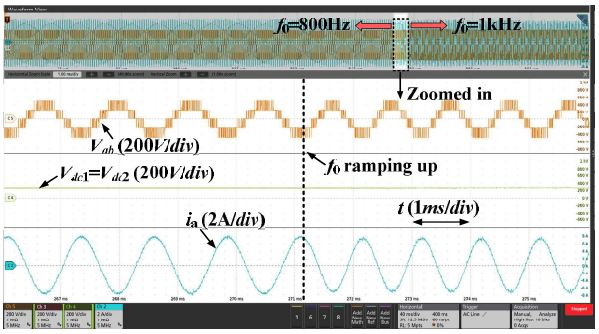

(b)

Fig. 19. The transient-state modulation performance of the proposed hybrid active PWM strategy under a step change of: (a) MI and (b) f_0.

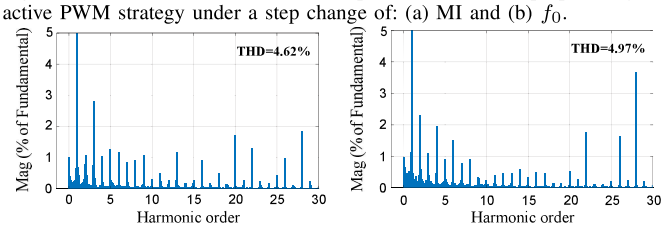

(a) (b)

Fig. 20. Harmonic spectrum of phase current at the steady state with: (a) C-mode and (b) D-mode.

B. Steady-State Performance

In order to evaluate the steady-state performance of the proposed hybrid PWM strategy, tests are conducted under f_0 of 400 Hz and 1 kHz that correspond to the target drive systems operating in the startup process and in thrust generation, respectively. The former employs the active modulation waves formulating continuous switching patterns, whereas the latter transits to discontinuous pulse trains to lower power losses, aiming for high-efficiency electric propulsion. It can be seen from Fig.18 that two capacitor voltages are maintained at a balanced condition under both aforementioned operating points, also with sinusoidal phase currents.

C. Transient-State Performance

As the propulsive loads and the machine speed may change during the flight, the following experiments are hence carried out to verify the D-mode modulation transient-state performance. Fig.19(a) shows that MI increases from 0.4 to 0.9, whilst Fig.19(b) displays an instant that the f_0 raises from 800 Hz to 1 kHz. These results demonstrate a good dynamic performance of the proposed hybrid PWM when the studied TeDP system experiences a step-change in loads and speed.

D. Distortion Analysis

Using FFT analysis on phase current, the THD with the conventional CBPWM and NTV^2-based CBPWM schemes

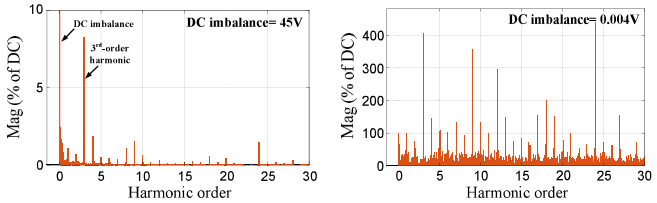

(a) (b)

Fig. 21. Harmonic spectrum of NP potential at the steady state with: (a) The conventional CBPWM (b) The proposed hybrid active PWM with D-mode.

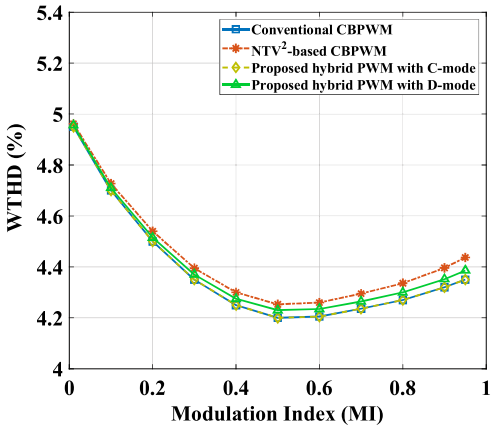

Fig. 22. WTHD of the line-to-line voltage with the benchmark method and the proposed hybrid active PWM algorithm with dual-mode modulation waves.

are obtained. When the target systems operate under a MI of 0.95, PF of 0.75 and f_0 of 1 kHz, denoting the steady-state, the value for the benchmark method are 4.56% and 5.43%, respectively. In contrast, the THD with the proposed hybrid active PWM strategy with the C-mode and D-mode are 4.62% and 4.97%, respectively. Besides, harmonic components for this situation are presented in Fig.20. As shown, the continuous switching pattern results in evenly distributed harmonics spectra, while its D-mode counterpart mainly clusters around low-order harmonics as five-segment pulse trains are dominantly generated to approximate reference voltage command. Fig.21 gives the spectrum of NP potential, in which the low-frequency fluctuation, particularly the 3^{rd}-order harmonics, has been effectively eliminated by the proposed hybrid active PWM under its D-mode formation, as opposed to the original CBPWM scheme. Fig.21 shows the weighted THD (WTHD) comparison of the line-to-line voltage under the benchmark method and the proposed algorithm at different modulation indices. As can be seen, the WTHD of the presented PWM technique with C-mode modulation signals almost overlaps with that of the CBPWM scheme while its D-mode counterpart causes a higher WTHD. However, because of additional three-level switching intervals, the value of the NTV^2-CBPWM scheme renders the highest WTHD during the entire operating points of the investigated propulsion drives.

E. Computational Performance

The execution time of the proposed modulation strategy including the benchmark methods are all implemented in the dSPACE and their execution times are measured in the real-time mode. The test results show that it costs 14.8μs to execute the presented hybrid active PWM. Compared with the SVM implementation with 18.3μs, the computation sources are significantly saved by 23.6%. The performance is also

acceptable in contrast with that of the conventional CB and the NTV^2-based CB implementations with 13.7μs and 14.1μs.

VI. Conclusion

In this paper, a new hybrid active PWM technique with dual-mode modulation waves has been proposed for a 3-L T^{2}C exploited in the next-generation aircraft TeDP systems. With the help of the sextant coordinates, the modulated signals are comprised by two simple control variables, thereby evolving dual-mode pulse trains. Besides, the capacitor voltage balancing and switching loss reduction are realized by the introduced modulation approach at the same time. The major contributions of this work lie in the following: 1) The equivalence of the NTV and CBPWM strategy is well elucidated based on the sextant-coordinate system; 2) The space-domain oriented ZSVs are derived, which merges the characteristics of space-vectors into modulation signals effectively; 3) Dedicated DPWM with NP voltage error correction and ripple mitigation is achieved by the presented hybrid active PWM, which especially aims for the operating points at the cruising stage; 4) By leveraging programmable reference voltage vector vertices and their projected ZSVs, this PWM algorithm can bring simplicity as well as an extra degree of freedom. The provided PWM strategy can also apply to other 3L-NPC topologies and establish a cornerstone in future MW-class high power density motor drives for electric aircraft propulsion applications. Simulation and experimental results both confirmed the good overall modulation performance of the proposed PWM solution in terms of NP voltage balancing, power losses, ease of use and high scalability.

References

[1] G. Buticchi, P. Wheeler and D. Boroyevich, "The more-electric aircraft and beyond," *Proc. IEEE.*, vol. 2, no. 4, pp. 6-12, Dec. 2014.

[2] S. Sirimanna, T. Balachandran, N. Salk, J. Xiao, D. Lee and K. Haran, "Electric propulsors for zero-emission aircraft: partially superconducting machines," *Proc. IEEE.*, vol. 8, no. 2, pp. 18-26, Jun. 2020.

[3] P. Wheeler, T. S. Sirimanna, S. Bozhko and K. S. Haran, "Electric/hybrid-electric aircraft propulsion systems," *Proc. IEEE*, vol. 109, no. 6, pp. 1115-1127, Jun. 2021.

[4] M. Ghassemi, A. Barzkar and M. Saghafi, "All-electric NASA N3-X aircraft electric power systems," *IEEE Trans. Transport. Electrific.*, vol. 8, no. 4, pp. 4091-4104, Dec. 2022.

[5] "STARC-ABL" NASA Glenn Research Center. [Online]. Available: https://www1.grc.nasa.gov/aeronautics/eap/airplane-concepts/starc-abl/

[6] D. Golovanov *et al.*, "4-MW class high-power-density generator for future hybrid-electric aircraft," *IEEE Trans. Transport. Electrific.*, vol. 7, no. 4, pp. 2952-2964, Dec. 2021.

[7] E. Sayed *et al.*, "Review of electric machines in more-/hybrid-/turbo-electric aircraft," *IEEE Trans. Transport. Electrific.*, vol. 7, no. 4, pp. 2976-3005, Dec. 2021.

[8] A. Trentin *et al.*, "Research and realization of high-power medium-voltage active rectifier concepts for future hybrid-electric aircraft generation," *IEEE Trans. Ind. Electron.*, vol. 68, no. 12, pp. 11684-11695, Dec. 2021.

[9] D. Zhang, J. He and D. Pan, "A megawatt-scale medium-voltage high-efficiency high power density "SiC+Si" hybrid three-level ANPC inverter for aircraft hybrid-electric propulsion systems," *IEEE Trans. Ind. Appl.*, vol. 55, no. 6, pp. 5971-5980, Nov.-Dec. 2019.

[10] J. Shen, S. Schröder, R. Rösner, and S. El-Barbari, "A comprehensive study of neutral-point self-balancing effect in neutral-point-clamped three-level inverters," *IEEE Trans. Power Electron*, vol. 26, no. 11, pp. 3084-3095, Nov. 2011.

[11] R. Sommer, A. Mertens, C. Brunotte and G. Trauth, "Medium voltage drive system with NPC three-level inverter using IGBTs," in *Proc. IEEE PWM Medium Voltage Drives Semin.*, May 11, 2000, pp. 3/1-3/5.

[12] S. Busquets-Monge, J. Bordonau, D. Boroyevich and S. Somavilla, "The nearest three virtual space vector PWM—a modulation for the comprehensive neutral-point balancing in the three-level NPC inverter," *IEEE Power Electron. Lett.*, vol. 2, no. 1, pp. 11-15, Mar. 2004.

[13] A. Choudhury, P. Pillay, and S. S. Williamson, "DC-bus voltage balancing algorithm for three-level neutral-point-clamped (NPC) traction inverter drive with modified virtual space vector," *IEEE Trans. Ind. Appl.*, vol. 52, no. 5, pp. 3958-3967, Sep./Oct. 2016.

[14] C. Xiang, C. Shu, D. Han, B. Mao, X. Wu and T. Yu, "Improved virtual space vector modulation for three-level neutral-point-clamped converter with feedback of neutral-point voltage," *IEEE Trans. Power Electron.*, vol. 33, no. 6, pp. 5452-5464, Jun. 2018.

[15] F. Guo *et al.*, "An overmodulation algorithm with neutral-point voltage balancing for three-level converters in high-speed aerospace drives," *IEEE Trans. Power Electron.*, vol. 37, no. 2, pp. 2021-2032, Feb. 2022.

[16] S. Xia, X. Wu, J. Zheng, X. Li and K. Wang, "A virtual space vector PWM with active neutral point voltage control and common mode voltage suppression for three-level NPC converters," *IEEE Trans. Ind. Electron.*, vol. 68, no. 12, pp. 11761-11771, Dec. 2021.

[17] W. Jiang *et al.*, "A novel virtual space vector modulation with reduced common-mode voltage and eliminated neutral point voltage oscillation for neutral point clamped three-level inverter," *IEEE Trans. Ind. Electron.*, vol. 67, no. 2, pp. 884-894, Feb. 2020.

[18] F. Guo, T. Yang, A. M. Diab, S. S. Yeoh, S. Bozhko and P. Wheeler, "An enhanced virtual space vector modulation scheme of three-level NPC converters for more-electric-aircraft applications," *IEEE Trans. Ind. Appl.*, vol. 57, no. 5, pp. 5239-5251, Sept.-Oct. 2021.

[19] T. Yu *et al.*, "A modulation method to eliminate leakage current and balance neutral-point voltage for three-level inverters in photovoltaic systems," *IEEE Trans. Ind. Electron.*, doi: 10.1109/TIE.2022.3161809.

[20] F. Guo *et al.*, "Hybrid active modulation strategy for three-level neutral-point-clamped converters in high-speed aerospace drives," *IEEE Trans. Ind. Electron.*, vol. 70, no. 4, pp. 3449-3460, Apr. 2023.

[21] M. Lak, Y. -T. Tsai, B. -R. Chuang, T. -L. Lee and M. H. Moradi, "A hybrid method to eliminate leakage current and balance neutral point voltage for photovoltaic three-level T-type inverter," *IEEE Trans. Power Electron.*, vol. 36, no. 10, pp. 12070-12089, Oct. 2021.

[22] H. Lin *et al.*, "Fuzzy sliding-mode control for three-level NPC AFE rectifiers: a chattering alleviation approach," *IEEE Trans. Power Electron.*, vol. 37, no. 10, pp. 11704-11715, Oct. 2022.

[23] Y. Yang *et al.*, "An efficient model predictive control using virtual voltage vectors for three-phase three-level converters with constant switching frequency," *IEEE Trans. Ind. Electron.*, vol. 69, no. 4, pp. 3998-4009, Apr. 2022.

[24] P. Liu, S. Duan, C. Yao and C. Chen, "A double modulation wave CBPWM strategy providing neutral-point voltage oscillation elimination and CMV reduction for three-level NPC inverters," *IEEE Trans. Ind. Electron.*, vol. 65, no. 1, pp. 16-26, Jan. 2018.

[25] N. Beniwal *et al.*, "A dual-mode modulation technique for controlling the average neutral point current in neutral-point-clamped converters," *IEEE Trans. Power Electron.*, vol. 36, no. 5, pp. 6079-6091, May 2021.

[26] N. Beniwal *et al.*, "Dual-layer pulsewidth modulation technique for average neutral point current control in neutral-point-clamped converters," *IEEE Trans. Power Electron.*, vol. 37, no. 10, pp. 11762-11773, Oct. 2022.

[27] W. Jiang *et al.*, "A carrier-based discontinuous PWM strategy for T-type three-level converter with reduced common mode voltage, switching loss, and neutral point voltage control," *IEEE Trans. Power Electron.*, vol. 37, no. 2, pp. 1761-1771, Feb. 2022.

[28] S. Mukherjee, S. K. Giri, and S. Banerjee, "A flexible discontinuous modulation scheme with hybrid capacitor voltage balancing strategy for three-level NPC traction inverter," *IEEE Trans. Ind. Electron.*, vol. 66, no. 5, pp. 3333-3343, May 2019.

[29] S. K. Giri, S. Mukherjee, S. Kundu, S. Banerjee, and C. Chakraborty, "An improved PWM scheme for three-level inverter extending operation into overmodulation region with neutral-point voltage balancing for full power-factor range," *IEEE J. Emerg. Sel. Topics Power Electron.*, vol. 6, no. 3, pp. 1527-1539, Sep. 2018.

[30] J. Lee, S. Yoo and K. Lee, "Novel discontinuous PWM method of a three-level inverter for neutral-point voltage ripple reduction," *IEEE Trans. Ind. Electron.*, vol. 63, no. 6, pp. 3344-3354, Jun. 2016.

[31] A. Choudhury, P. Pillay and S. S. Williamson, "A hybrid PWM-based DC-link voltage balancing algorithm for a three-level NPC DC/AC traction inverter drive," *IEEE J. Emerg. Sel. Topics Power Electron.*, vol. 3, no. 3, pp. 805-816, Sept. 2015.

[32] K. Li *et al.*, "Triangle carrier-based DPWM for three-level NPC inverters," *IEEE J. Emerg. Sel. Topics Power Electron.*, vol. 6, no. 4, pp. 1966-1978, Dec. 2018.

[33] Q. Yan, Z. Zhou, M. Wu, X. Yuan, R. Zhao and H. Xu, "A simplified analytical algorithm in *abc* coordinate for the three-level SVPWM," *IEEE Trans. Power Electron.*, vol. 36, no. 4, pp. 3622-3627, Apr. 2021.
[34] Z. Gao, Q. Ge, Y. Li, L. Zhao, B. Zhang and K. Wang, "Hybrid improved carrier-based PWM Strategy for three-level neutral-point-clamped inverter with wide frequency range," *IEEE Trans. Power Electron.*, vol. 36, no. 7, pp. 8517-8538, Jul. 2021.
[35] W. Jiang, L. Wang, J. Wang, X. Zhang, and P. Wang, "A carrier-based virtual space vector modulation with active neutral-point voltage control for a neutral-point-clamped three-level inverter," *IEEE Trans. Ind. Electron.*, vol. 65, no. 11, pp. 8687-8696, Nov. 2018.
[36] F. Guo, T. Yang, C. Li, S. Bozhko and P. Wheeler, "Active modulation strategy for capacitor voltage balancing of three-level neutral-point-clamped converters in high-speed drives," *IEEE Trans. Ind. Electron.*, vol. 69, no. 3, pp. 2276-2287, Mar. 2022.
[37] F. Guo, Y. Zhao and P. Wheeler, "A CBPWM strategy with flexible zero-sequence voltage injection for three-level TNPC converters in aircraft electric starter/generator system," in *Proc. IEEE Energy Convers. Congr. Expo.*, Detroit, MI, USA, Oct. 2022, pp. 1-6. doi: 10.1109/ECCE50734.2022.9947425.

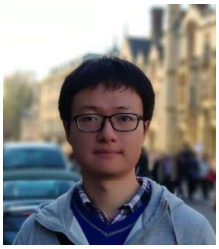

Feng Guo (Member, IEEE) received his B.Eng. from China University of Mining and Technology, Xuzhou, China, in 2014, and received M.S. (Hons.) from Northeastern University, Shenyang, China, in 2017, both in electrical engineering, and the Ph.D. degree at the Power Electronics, Machines and Control (PEMC) Group in electrical and electronics engineering from the University of Nottingham, Nottingham, U.K., in 2021.

Since January 2022, he has been with the Power Electronic Systems Laboratory at Arkansas (PESLA), University of Arkansas, Fayetteville, AR, USA, as a Postdoctoral Research Fellow. From 2016 to 2017, he was a visiting student at the Chinese University of Hong Kong, Shenzhen, China. His research interests include pulse-width-modulation strategy, high efficiency and high power-density multilevel converters, wide bandgap power device applications, high-speed motor drives and transportation electrification, etc. He was the recipient of the 2017 Outstanding Graduate Student Award and the 2022 IEEE Industry Applications Society (IAS) Transactions Second Place Prize Paper Award.

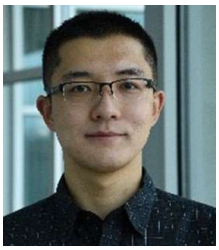

Zhuxuan Ma (Student Member, IEEE) received the B.S. degree in electrical engineering from the Beijing Institute of Technology, Beijing, China, in 2017, and the M.S. degree from The Ohio State University, Columbus, OH, USA, in 2019. He is currently pursuing the Ph.D. degree with the Department of Electrical Engineering, University of Arkansas, Fayetteville, AR, USA. He was a Power Electronics Systems Intern in Electronics & Fuel Systems, Cummins Ins., Fridley, MN, USA, in 2022.

His current research interests include wide bandgap power semiconductor devices characterization and application and power electronics converters.

Fei Diao (Member, IEEE) received the B.E. and M.E. degrees in electrical engineering from Southwest Jiaotong University, Chengdu, China, in 2015 and 2018, and received the Ph.D. degree in electrical engineering from University of Arkansas, Fayetteville, USA, in 2022. Since 2022, he has been working as a Senior Power Electronics Control System Engineer for John Deere, Cary, NC, USA.

His current research interests include motor control, modulation and control of power converters, wide bandgap power applications.

Yue Zhao (Senior Member, IEEE) received a B.S. degree in electrical engineering from Beijing University of Aeronautics and Astronautics, Beijing, China, in 2010, and a Ph.D. degree in electrical engineering from the University of Nebraska-Lincoln, Lincoln, USA, in 2014. He was an Assistant Professor in the Department of Electrical and Computer Engineering at the Virginia Commonwealth University, Richmond, USA, in 2014-2015. Since August 2015, he has been with the University of Arkansas (UA), Fayetteville, USA, where he is currently an Associate Professor in the Department of Electrical Engineering. He also serves as the Executive Director for the National Science Foundation (NSF) I/UCRC on GRid-connected Advanced Power Electronic Systems (GRAPES). His current research interests include electric machines and drives, power electronics, and renewable energy systems. He has 4 U.S. patents granted and co-authored more than 130 papers in refereed journals and international conference proceedings. Dr. Zhao is an Associated Editor of the IEEE Transactions on Industry Applications and IEEE Open Journal of Power Electronics. He was a recipient of 2018 NSF CAREER Award, the 2020 IEEE Industry Applications Society Andrew W. Smith Outstanding Young Member Achievement Award and the 2020 UA College of Engineering Dean's Award of Excellence.

Patrick Wheeler (Fellow, IEEE) received his BEng [Hons] degree in 1990 from the University of Bristol, UK. He received his PhD degree in Electrical Engineering for his work on Matrix Converters from the University of Bristol, UK in 1994. In 1993 he moved to the University of Nottingham and worked as a research assistant in the Department of Electrical and Electronic Engineering. In 1996 he became a Lecturer in the Power Electronics, Machines and Control Group at the University of Nottingham, UK. Since January 2008 he has been a Full Professor in the same research group. He is currently the Global Engagement Director For the Faculty of Engineering, the Head of the Power Electronics, Machines and Control Research Group and the Director of the University of Nottingham's Institute of Aerosapce Technology He was Head of the Department of Electrical and Electronic Engineering at the University of Nottingham from 2015 to 2018. He is a member of the IEEE PELs AdCom and is currently IEEE PELS Vice-President for Technical Operations. He has published over 850 academic publications in leading international conferences and journals.

Yue Cao (Senior Member, IEEE) received the B.S. degree (Hons.) in electrical engineering with a second major in mathematics from the University of Tennessee, Knoxville, TN, USA, in 2011, and the M.S. and Ph.D. degrees in electrical engineering from the University of Illinois at Urbana-Champaign (UIUC), Champaign, IL, USA, in 2013 and 2017, respectively.

Dr. Cao is currently an Assistant Professor with the Energy Systems Group at Oregon State University (OSU), Corvallis, OR, USA. Before joining OSU, he was a Research Scientist with the Propulsions Team at Amazon Prime Air in Seattle, WA, USA. He was a Power Electronics Engineer Intern with Special Projects Group at Apple Inc., Cupertino, CA, USA; Halliburton Company, Houston, TX, USA; and Oak Ridge National Laboratory, TN, USA. He was a Sundaram Seshu Fellow in 2016 at UIUC, where he was a James M. Henderson Fellow in 2012. His research interests include power electronics, motor drives, and energy storage with applications in renewable energy integration and transportation electrification.

Dr. Cao was a national finalist of the USA Mathematical Olympiad (USAMO) in 2006 and 2007. He received the Myron Zucker Student Award from the IEEE Industry Applications Society (IAS) in 2010. He won the Oregon State Learning Innovation Award for transformative education in 2020. He is a recipient of the 2022 NSF CAREER award. He is selected into U.S. National Academy of Engineering (NAE) Frontiers of Engineering (FOE) Class of 2022. He received the annual OSU Promising Scholar Award in 2023. Dr. Cao was the Tutorials Chair and Special Sessions Chair of the 2021-2022 IEEE Energy Conversion Congress Expo (ECCE). He is Vice Chair of IEEE Power Electronics Society (PELS) TC11-Aerospace Power. He is currently an Associate Editor for IEEE Transactions on Transportation Electrification and an Associate Editor for IEEE Transactions on Industry Applications.